PAPER

Particle detachment from fluid interfaces: theory vs. experiments†

Svetoslav E. Anachkov,‡[ab] Ivan Lesov,‡[ab] Michele Zanini,[a] Peter A. Kralchevsky,[b] Nikolai D. Denkov[b] and Lucio Isa*[a]

Microparticle adsorption and self-assembly at fluid interfaces are strongly affected by the particle three-phase contact angle θ. On the single-particle level, θ can be determined by several techniques, including colloidal-probe AFM, the gel-trapping technique (GTT) and the freeze-fracture shadow-casting (FreSCa) method. While GTT and FreSCa provide contact angle distributions measured over many particles, colloidal-probe AFM measures the wettability of an individual (specified) particle attached onto an AFM cantilever. In this paper, we extract θ for smooth microparticles through the analysis of force–distance curves upon particle approach and retraction from the fluid interface. From each retraction curve, we determine: (i) the maximal force, F_{max}; (ii) the detachment distance, D_{max}; and (iii) the work for quasi-static detachment, W. To relate F_{max}, D_{max} and W to θ, we developed a detailed theoretical model based on the capillary theory of flotation. The model was validated in three different ways. First, the contact angles, evaluated from F_{max}, D_{max} and W, are all close in value and were used to calculate the entire force–distance curves upon particle retraction without any adjustable parameters. Second, the model was successfully applied to predict the experimental force–distance curve of a truncated sphere, whose cut is positioned below the point of particle detachment from the interface. Third, our theory was confirmed by the excellent agreement between the particle contact angles obtained from the colloidal-probe AFM data and the ensemble-average contact angles measured by both GTT and FreSCa. Additionally, we devised a very accurate closed-form expression for W (representing the energy barrier for particle detachment), thus extending previous results in the literature.

1. Introduction

Particle adsorption and self-assembly at fluid interfaces have attracted considerable attention as these phenomena can be exploited in a vast range of materials and processes, including Pickering-stabilized emulsions and foams,[1,2] drug-delivery vehicles,[3,4] mineral recovery by flotation[5] and fabrication of nanostructured materials.[6–11] One of the main parameters controlling the particle interfacial behavior is its three-phase contact angle θ. Commonly, θ is defined as the angle of the tangent to the particle surface at the three-phase contact line, measured through the aqueous phase; therefore, we have $\theta < 90°$ for hydrophilic particles and $\theta > 90°$ for hydrophobic particles. The binding energy, ΔG, of a solid spherical colloid

with radius R attached to a fluid interface with interfacial tension σ is given by $\Delta G = -\pi R^2 \sigma (1 - |\cos\theta|)^2$; see ref. 12 and 13. Therefore, for microparticles with typical contact angles ($\theta = 45°–135°$), the adsorption is practically irreversible since $|\Delta G| > 10^6 k_B T$. By controlling particle immersion in each fluid phase, θ also affects particle self-assembly[14] and dynamics[15,16] at the interface. Furthermore, interparticle interactions, *e.g.*, capillary[17] forces that arise due to interfacial deformations around each particle, depend on particle wettability, *i.e.* on θ.

Different techniques have been developed to obtain θ for colloidal particles,[18] based on direct visualization[19–23] or indirect measurements.[24–30] The gel-trapping technique (GTT)[19,20] and freeze-fracture shadow-casting (FreSCa) cryo-SEM[21,22] are applicable for contact-angle measurements of nano- and microparticles. FreSCa can be used only for oil–water interfaces, whereas GTT is applicable to both air–water and oil–water interfaces. Alternatively, for micron-sized particles at the air–water interface, θ can be measured directly by entrapping them in a poly-(butylcyanoacrylate) film.[23] For hydrophilic micrometer-sized particles, additional methods include contact-angle determination by optical microscopy using the film-trapping technique[24]

[a] *Laboratory for Interfaces, Soft matter and Assembly, Department of Materials, ETH Zurich, Vladimir-Prelog-Weg 5, CH-8093 Zurich, Switzerland. E-mail: lucio.isa@mat.ethz.ch; Tel: +41 44 633 63 76*

[b] *Department of Chemical and Pharmaceutical Engineering, Faculty of Chemistry and Pharmacy, Sofia University, 1 James Bourchier Ave., 1164 Sofia, Bulgaria*

† Electronic supplementary information (ESI) available: Appendix A: additional figures, derivations and comments. See DOI: 10.1039/c6sm01716a

‡ Both authors contributed equally.

or the film-caliper method.[25] Finally, θ can also be evaluated from global interfacial properties by applying appropriate theoretical models. For instance, using a Langmuir trough,[26] θ can be estimated from the pressure–area-isotherms differences between a surfactant and a surfactant–particle system, assuming there are no surfactant–particle interactions. Alternatively, using an ellipsometer[27,28] and applying a two-layer model to describe a particle–laden interface, one can deduce the average particle position relative to the interface and then calculate θ.

The methods described above can be applied to measure contact angles either on a single-particle level,[19–25] or to obtain an average[26–28] value. Yet, none of these techniques permits direct force measurements associated with particle attachment and detachment – both related to θ. The only available method that does not impose any major restrictions in terms of the choice of both particles and fluids is colloidal-probe AFM.[29–31] In general, by colloidal-probe AFM one measures the interaction forces between a probe particle and a surface as a function of separation, commonly referred to as force–distance curves (see Fig. 1a). The latter can provide valuable information on local material properties such as elasticity, adhesion and even surface charge densities.[32]

In this work, we apply colloidal-probe AFM to measure the interactions between colloidal particles and a fluid interface. More specifically, we attach smooth micron-sized silica particles to AFM cantilevers and measure their interactions with air–water and oil–water interfaces as a function of particle size and particle surface modification. The experimental data are analyzed using a detailed and self-consistent theoretical model, which relates θ to various measurable quantities. As demonstrated below, our model can predict the entire force–distance curves describing particle detachment without any adjustable parameters. To verify our results for θ, we compare them to contact-angle measurements from independent

experimental methods such as GTT and FreSCa. The excellent agreement proves that our theoretical model is correct and self-consistent, and can be used to determine θ from AFM experimental data.

2. Theory

2.1. Theoretical background

Here, we present briefly the basic theoretical equations that describe the detachment of solid spherical particles from fluid interfaces. The geometrical representation in Fig. 1b depicts a solid sphere attached to an AFM cantilever at the oil–water (or air–water) interface. For a micrometer-sized particle (negligible particle weight and buoyancy) in its equilibrium position at the interface, the fluid–fluid phase boundary is flat and the net force acting on the particle is 0. By pulling the particle upwards, however, the interface deforms, which gives rise to a capillary force, F, acting on the colloidal probe. Due to the axial symmetry of the system, there is a net capillary force only in the vertical direction:

$$f \equiv \frac{F}{2\pi R\sigma} = \sin\alpha\sin(\theta - \alpha), \tag{1}$$

where f is the dimensionless capillary force; R is the particle radius; σ is the interfacial tension of the fluid interface; θ is the three-phase contact angle; and α is the central angle (Fig. 1b). During the detachment process, the capillary force balances out the upward (pulling) force; hence, f acts downwards and is considered negative in our reference system. Describing the detachment process, two different conditions for the three-phase contact line are possible: either the contact line does not move until a threshold force is reached (pinned contact line) or it moves smoothly over the particle surface maintaining a constant contact angle (sliding contact line). We only focus on the latter case – sliding contact line and constant contact angle, for which
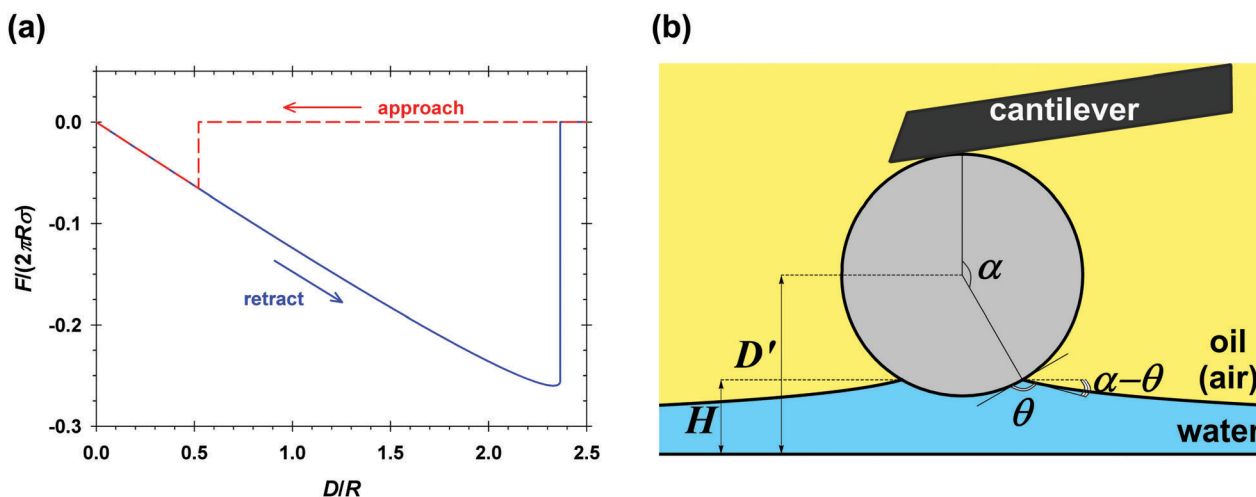
Fig. 1 (a) Schematic representation of an approach and retraction force–distance curve experiment in normalized units. (b) Sketch of a colloidal sphere attached onto an AFM cantilever that deforms a fluid interface. Here, α is the central angle and θ is the three-phase contact angle measured through the aqueous phase; D' is the distance between the particle center of mass and the unperturbed (flat) fluid interface at a large distance from the particle; and H is the meniscus height.

the capillary force passes through a minimum and its maximal (in magnitude) value yields:[33,34]

$$f_{max} \equiv \frac{F_{max}}{2\pi R\sigma} = \cos^2 \frac{\theta}{2}, \tag{2}$$

This value is reached when the central angle α becomes equal to $\alpha_{max,1} = (\pi + \theta)/2$, which happens during pulling of the particle away from the interface.

The detachment process is also characterized by the distance, D, between the particle center of mass and its equilibrium position expressed by:

$$d \equiv \frac{D}{R} = \frac{D'}{R} + \cos\theta = \frac{H}{R} - \cos\alpha + \cos\theta, \tag{3}$$

where d denotes the respective dimensionless distance, which is equal to zero when the particle is in its equilibrium position at the interface ($\alpha = \theta$, $H = 0$); D' is the distance between the particle center of mass and the unperturbed (flat) interface; and H stands for the meniscus rise around the sphere. The latter can be calculated using an approximate analytical formula, which reads:[34]

$$h \equiv \frac{H}{R} = \sin\alpha \sin(\alpha - \theta) \left[\ln\frac{4}{\varepsilon \sin\alpha(1 + \cos(\alpha - \theta))} - \gamma \right], \tag{4}$$

$$\varepsilon \ll 1$$

where:

$$\varepsilon \equiv qR, \quad q = \sqrt{\frac{\Delta\rho g}{\sigma}}. \tag{5}$$

Here, h is the dimensionless meniscus height; $\gamma \approx 0.5772$ is the Euler–Mascheroni constant; ε is the dimensionless Bond number; q^{-1} is the capillary length; $\Delta\rho$ is the density difference between the two fluid phases; and $g \approx 9.80665$ m s^{-2} is the standard value for the acceleration due to gravity. It is important to point out that the formula in eqn (4) holds when $\varepsilon \ll 1$. Originally, the formula was derived for the meniscus rise around a thin cylinder (needle) by Derjaguin[35] and was later extended using matched asymptotic expansions.[36–38]

For a given θ and $\varepsilon = qR$, the dimensionless force–distance curve $f(d)$ can be calculated in the parametric form: $f = f(\alpha, \theta)$ using eqn (1) and $d = d(\alpha, \theta, \varepsilon)$ using eqn (3). Note that at fixed values of θ and ε, the functions $|f(\alpha)|$ and $d(\alpha)$ have maxima, which will be denoted by $\alpha_{max,1}$ and $\alpha_{max,2}$, respectively; see Fig. 2a. These maxima have the following physical meaning.

Let us consider a particle that is fixed to the cantilever (Fig. 1b). The particle is slowly (quasistatically) pulled upwards, so that the contact line slides downwards relative to the particle surface. By imposing different regimes on the cantilever, this quasistatic process can be carried out in two different ways.

(i) Force control: the force magnitude $|f|$, acting on the cantilever, is gradually increased with time, and correspondingly, α and d increase in accordance with eqn (1) and (3). In such a case, the particle detaches when the force becomes equal to f_{max} and the central angle is $\alpha = \alpha_{max,1}$.

(ii) Displacement control: the distance d is gradually increased with time, and then, α and f vary in accordance with
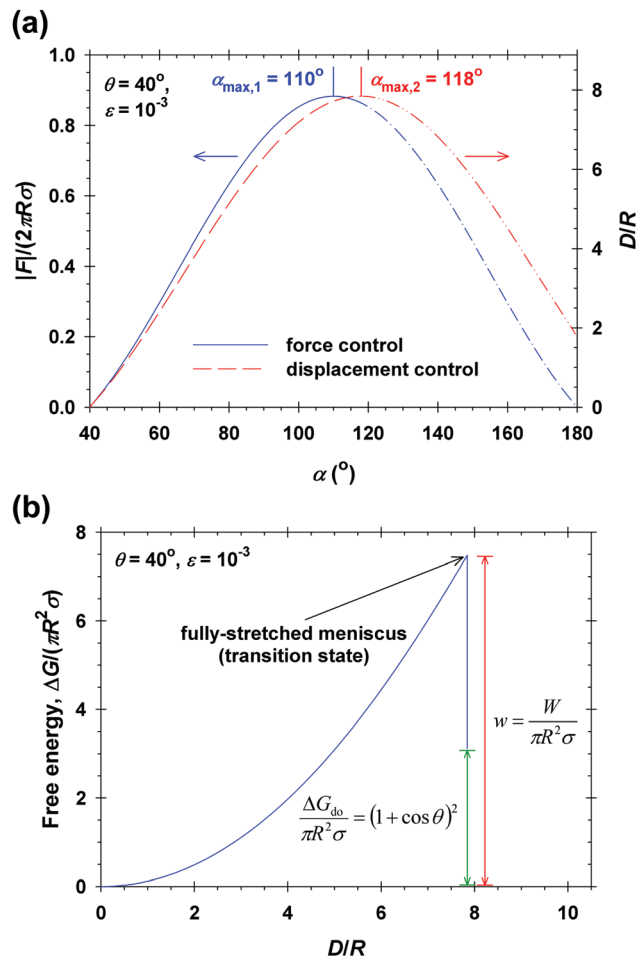

Fig. 2 (a) Plots of $|F|/(2\pi R\sigma)$ and D/R vs. the central angle α. These two curves exhibit maxima at different α values denoted by $\alpha_{max,1}$ and $\alpha_{max,2}$, respectively. The dash-dotted lines correspond to the unstable branches after particle detachment. (b) Plot of $\Delta G/(\pi R^2\sigma)$ vs. D/R, which shows that W represents the energy barrier for particle detachment and ΔG_{do} is the change in free energy for particle detachment into the oil (or upper) phase. Here, the equilibrium position of the particle at the fluid interface is chosen as a reference state for ΔG.

eqn (3) and (1). At $\alpha = \alpha_{max,1}$, the maximal force is reached, but the particle remains attached. Upon further increase of d, the force decreases. At $d = d_{max} \equiv D_{max}/R$ (see Fig. 2a), corresponding to $\alpha = \alpha_{max,2}$, the particle detaches.

To sum up, the particle will detach at either $\alpha = \alpha_{max,1}$, or $\alpha = \alpha_{max,2}$, depending on whether the cantilever motion is carried out under force or displacement control. It should be noted that our experiments were performed under displacement control.

The area over the $F(D)$ curve is equal to the work for particle detachment W. Physically, W represents the energy barrier for particle detachment into the upper phase (see Fig. 2b) and is analogous to the activation energy of chemical reactions. W is evaluated as follows:

$$w \equiv \frac{W}{\pi R^2\sigma} = -2\int_0^{d_i} f\,dd = 2\int_\theta^{\alpha_{max,i}} \sin\alpha \sin(\alpha - \theta)\left[\frac{dh}{d\alpha} + \sin\alpha\right]d\alpha, \tag{6}$$

where w is the dimensionless work for particle detachment; $d_i = d(\alpha_{\max,i}, \theta, \varepsilon)$; and $i = 1$ or 2.

In the case of force control, the particle detaches from the interface at $\alpha = \alpha_{\max,1} = (\pi + \theta)/2$ and w can be calculated analytically. Pitois & Chateau[39,40] were the first to find an exact formula, hereby denoted by w_{PC}:

$$
\begin{aligned}
w_{PC} &= 2 \int_\theta^{(\pi+\theta)/2} \sin\alpha \sin(\alpha - \theta) \left[\frac{dh}{d\alpha} + \sin\alpha \right] d\alpha \\
&= \left(1 - \sin\frac{\theta}{2}\right)^2 \left\{ \frac{1}{2}\left(7\sin^2\frac{\theta}{2} + 8\sin\frac{\theta}{2} + 3\right) \right. \\
&\quad \left. - \left(1 + \sin\frac{\theta}{2}\right)^2 \left(\ln\left[\frac{\varepsilon}{4}\cos\frac{\theta}{2}\left(1 + \sin\frac{\theta}{2}\right)\right] + \gamma \right) \right\}.
\end{aligned}
\tag{7}
$$

In the case of displacement control, the particle detaches from the interface at $\alpha = \alpha_{\max,2}$, when D is maximal. This case was first considered by Scheludko et al.[34] and W was evaluated numerically for particle detachment in the lower phase. Later, using perturbation methods, approximate closed-form formulae for $\alpha_{\max,2}$ and W were derived by Chateau & Pitois.[40] In Section 2.2, we propose more accurate expressions with wider ranges of applicability.

2.2. Extension of the theory

The expressions derived here are applicable to both flotation separation processes[34] and colloidal-probe AFM measurements that take place under displacement (distance) control. The starting point is the condition for maximal detachment distance $d_{\max} \equiv D_{\max}/R$:

$$
\frac{d}{d\alpha}(d(\alpha, \theta, \varepsilon)) = 0 \Rightarrow \alpha_{\max,2} = \alpha_{\max,2}(\theta, \varepsilon).
\tag{8}
$$

Eqn (8) is transcendental and can be solved numerically for any given θ and ε. In the interval $[0,\pi]$, there are two physically meaningful solutions for $\alpha_{\max,2}$ that satisfy eqn (8): (i) $\alpha_{\max,2} < \theta/2$, which corresponds to pushing downwards; and (ii) $\alpha_{\max,2} > (\pi + \theta)/2$, which corresponds to pulling upwards. Here, we are only interested in the latter case since it can be verified experimentally with our set-up. From the numerical solutions of eqn (8), we noticed that $\alpha_{\max,2}$ is close to $\alpha_{\max,1} = (\pi + \theta)/2$, so an approximate expression for $\alpha_{\max,2}$ is sought in the form:

$$
\alpha_{\max,2} \approx \frac{\pi + \theta}{2} + \delta\alpha_{\max,2}
\tag{9}
$$

where $\delta\alpha_{\max,2}$ is a small quantity. In view of eqn (3) and (9), the first order series expansion of eqn (8) has the form:

$$
\begin{aligned}
&\left.\frac{dh}{d\alpha}\right|_{\alpha=(\pi+\theta)/2} + \sin\left(\frac{\pi+\theta}{2}\right) + \left.\frac{d^2h}{d\alpha^2}\right|_{\alpha=(\pi+\theta)/2} \delta\alpha_{\max,2} \\
&\quad + \cos\left(\frac{\pi+\theta}{2}\right)\delta\alpha_{\max,2} \approx 0.
\end{aligned}
\tag{10}
$$

From eqn (4), after differentiation and some algebraic transformations, we derive:

$$
\begin{aligned}
&\left.\frac{dh}{d\alpha}\right|_{\alpha=\pi+\theta/2} = \cos\frac{\theta}{2}, \\
&\left.\frac{d^2h}{d\alpha^2}\right|_{\alpha=\pi+\theta/2} = 2\left\{1 + \gamma + \ln\left[\frac{\varepsilon}{4}\cos\frac{\theta}{2}\left(1 + \sin\frac{\theta}{2}\right)\right]\right\} - \sin\frac{\theta}{2}.
\end{aligned}
\tag{11}
$$

Substituting eqn (11) into eqn (10), we find:

$$
\delta\alpha_{\max,2} = \frac{\cos\dfrac{\theta}{2}}{\sin\dfrac{\theta}{2} - \ln\left[\dfrac{\varepsilon}{4}\cos\dfrac{\theta}{2}\left(1 + \sin\dfrac{\theta}{2}\right)\right] - \gamma - 1}.
\tag{12}
$$

Finally, a substitution of eqn (12) into eqn (9), yields:

$$
\alpha_{\max,2} \approx \frac{\pi + \theta}{2} + \frac{\cos\dfrac{\theta}{2}}{\sin\dfrac{\theta}{2} - \ln\left[\dfrac{\varepsilon}{4}\cos\dfrac{\theta}{2}\left(1 + \sin\dfrac{\theta}{2}\right)\right] - \gamma - 1}
\tag{13}
$$

At this point, we should mention that an approximation for $\alpha_{\max,2}$ was also found by Chateau & Pitois,[40] who used perturbation expansion in terms of the small parameter $1/\ln\varepsilon$. For the sake of comparison, we expand our result from eqn (13) in terms of $1/\ln\varepsilon$ and obtain:

$$
\begin{aligned}
\delta\alpha_{\max,2} &= \frac{-\cos\dfrac{\theta}{2}\dfrac{1}{\ln\varepsilon}}{1 - \left\{\sin\dfrac{\theta}{2} - \ln\left[\dfrac{1}{4}\cos\dfrac{\theta}{2}\left(1 + \sin\dfrac{\theta}{2}\right)\right] - \gamma - 1\right\}\dfrac{1}{\ln\varepsilon}} \\
&= -\cos\frac{\theta}{2}\left(\frac{1}{\ln\varepsilon}\right) \\
&\quad - \cos\frac{\theta}{2}\left\{\sin\frac{\theta}{2} - \ln\left[\frac{1}{4}\cos\frac{\theta}{2}\left(1 + \sin\frac{\theta}{2}\right)\right] - \gamma - 1\right\}\left(\frac{1}{\ln\varepsilon}\right)^2 + \dots
\end{aligned}
\tag{14}
$$

The first two terms in eqn (14) coincide with the result of Chateau & Pitois.[40] However, our result is more accurate since it contains the contributions of terms of order higher than $(1/\ln\varepsilon)^2$ and its derivation is much simpler.

Next, we will obtain the work $w^{(1)}$ for particle retraction under displacement control. First, it is useful to recast eqn (6) in the form:

$$
\Delta w^{(1)} \equiv w^{(1)} - w_{PC} = 2\int_{(\pi+\theta)/2}^{\alpha_{\max,2}} \Omega(\alpha)d\alpha,
$$
$$
\Omega(\alpha) = \sin\alpha \sin(\alpha - \theta)\left[\frac{dh}{d\alpha} + \sin\alpha\right]
\tag{15}
$$

Then, using the trapezoidal rule, we can estimate the integral from eqn (15) as follows:

$$
\begin{aligned}
2\int_{(\pi+\theta)/2}^{\alpha_{\max,2}} \Omega(\alpha)d\alpha &\approx 2\frac{\Omega\left(\dfrac{\pi+\theta}{2}\right) + \Omega(\alpha_{\max,2})}{2}\left(\alpha_{\max,2} - \frac{\pi+\theta}{2}\right) \\
&= 2\left(\alpha_{\max,2} - \frac{\pi+\theta}{2}\right)\cos^3\frac{\theta}{2},
\end{aligned}
\tag{16}
$$

where:

$$\Omega\left(\frac{\pi+\theta}{2}\right) = 2\cos^3\frac{\theta}{2}, \quad \Omega(\alpha_{\max,2}) = 0. \qquad (17)$$

The relation $\Omega(\alpha_{\max,2}) = 0$ follows from the fact that $\alpha_{\max,2}$ satisfies the condition for maximal particle displacement, eqn (8). Substituting eqn (13) and (16) into eqn (15), we get:

$$\Delta w^{(1)} \approx \frac{2\cos^4\frac{\theta}{2}}{\sin\frac{\theta}{2} - \ln\left[\frac{\varepsilon}{4}\cos\frac{\theta}{2}\left(1+\sin\frac{\theta}{2}\right)\right] - \gamma - 1}. \qquad (18)$$

The approximate closed-form formula for the work for quasistatic particle detachment under displacement control thus reads:

$$w^{(1)} = w_{PC} + \Delta w^{(1)} \qquad (19)$$

where w_{PC} is given by eqn (7) and $\Delta w^{(1)}$ by eqn (18). Again, to compare our expression for $w^{(1)}$ with the perturbation calculations of Chateau & Pitois,[40] we apply series expansion in terms of $1/\ln\varepsilon$:

$$
\begin{aligned}
\Delta w^{(1)} &= \frac{-2\cos^4\frac{\theta}{2}\frac{1}{\ln\varepsilon}}{1 - \left\{\sin\frac{\theta}{2} - \ln\left[\frac{1}{4}\cos\frac{\theta}{2}\left(1+\sin\frac{\theta}{2}\right)\right] - \gamma - 1\right\}\frac{1}{\ln\varepsilon}} \\
&= -2\cos^4\frac{\theta}{2}\left(\frac{1}{\ln\varepsilon}\right) \\
&\quad - 2\cos^4\frac{\theta}{2}\left\{\sin\frac{\theta}{2} - \ln\left[\frac{1}{4}\cos\frac{\theta}{2}\left(1+\sin\frac{\theta}{2}\right)\right] - \gamma - 1\right\} \\
&\quad \times \left(\frac{1}{\ln\varepsilon}\right)^2 + \dots \qquad (20)
\end{aligned}
$$

The first two terms in eqn (20) are similar to those in eqn (31) from ref. 40. Yet, two differences should be pointed out: (1) the prefactor $2\pi\sigma R_s^2$ is missing in eqn (31) of the reference due to a typographic error; and (2) the signs before the two $1/\ln\varepsilon$ terms should be minuses, not pluses. The latter error decreases the accuracy of eqn (31) from ref. 40 when compared to the exact numerical computations. As before, our formula for $w^{(1)}$ is more accurate since it incorporates the contributions of terms of order higher than $(1/\ln\varepsilon)^2$ and its derivation is straightforward.

3. Materials and methods

3.1. Materials

This study focuses on the wettability of microparticles at fluid interfaces. As model particles, we used: (i) monodisperse silica spheres with diameters 6.27 ± 0.23 μm and 7.38 ± 0.23 μm (Microparticles GmbH, Germany); and (ii) polydisperse silica spheres with diameters between 2 and 20 μm (MSS-500; Kobo Products Inc., USA). To investigate the effect of surface chemistry on the particle wetting properties, we compared non-modified and hydrophobized silica spheres. The surface hydrophobization was carried out using 1H,1H,2H,2H-perfluorooctyltriethoxysilane (98%, Sigma-Aldrich, Germany). As the oil phase, we used n-hexadecane (>99%, Sigma-Aldrich, Germany) in both AFM

and GTT experiments, whereas we used n-decane (>99%, Sigma-Aldrich, Germany) in FreSCa experiments. Both alkanes were purified from surface-active contaminants using an alumina column (MP EcoChrome™ Alumina B, Activity: Super I; MP Biomedicals, USA). The equilibrium interfacial tension of n-hexadecane against water was 52.5 ± 0.5 mN m^{-1} at 25 °C, measured by the pendant drop method (DSA100; Krüss GmbH, Germany) and later used in the numerical calculations.

For particle trapping in GTT, we used gellan gum (AppliChem, Germany), which was purified from surface-active contaminants using a high-purity silica gel column (60 Å pores, 70–230 mesh; Fluka, Germany). The polydimethylsiloxane (PDMS) replica of the interface was created using Sylgard® 184 elastomer (10:1 base-to-curing-agent ratio by weight; Sigma-Aldrich, Germany), while the UV-glue replica was prepared using UV-curable glue (Norland Optical Adhesives 63, Norland Products Inc., USA). For particle spreading, we used isopropanol (≥99.5%, Fisher Chemical, USA), whereas for rinsing cantilevers and silicon wafers we used isopropanol, ethanol (≥99.8%, Fluka, Germany), and acetone (≥99.9%, Sigma-Aldrich, Germany). All solvents were used as received without further purification. For solution preparation and as the aqueous phase, we used high-purity MilliQ water.

3.2. Methods

Hydrophobization procedure. For the surface modification of the silica microparticles, we used 1H,1H,2H,2H-perfluorooctyltriethoxysilane (or briefly fluorosilane). A droplet of silica suspension was deposited on the bottom of a UV-ozone-cleaned glass petri dish and then dried. After that, the petri dish was introduced in a UV-ozone chamber (Boekel UV Cleaner, Model 135500; Boekel Industries Inc., USA) for 30 minutes. Next, the silica particles were hydrophobized in the presence of fluorosilane vapors for 90 minutes at 23 °C. Silicon wafers and colloidal probes for AFM were hydrophobized using the same procedure.

Atomic force microscopy (AFM). We used an AFM (Nanowizard® 3 BioScience AFM; JPK Instruments AG, USA) to measure the capillary force acting on a silica microparticle at the air–water or oil–water interface. The measurements were carried out following the procedure developed by Butt and co-workers.[29,41] Each colloidal particle was attached to a tipless cantilever with nominal spring constant of 7.4 or 40 N m^{-1} (All-In-One-Al-TL; BudgetSensors®, Bulgaria) using a micromanipulator and UV-curable glue (Norland Optical Adhesives 61, Norland Products Inc., USA). The actual particle diameter was measured *a posteriori* by scanning electron microscopy (SEM). The cantilevers with the attached colloidal probes were calibrated using the thermal-noise method,[42] which is claimed to yield below 10% error in spring-constant determination.[29] Before calibration, to avoid the initial thermal drift of the cantilever, the colloidal probe was fully immersed into the upper phase (air or n-hexadecane) and the laser was turned on for *ca.* 60 minutes.

All force measurements were conducted in a liquid cell at 25 °C. The cell consisted of a truncated metal cone (1.5 mm height and 2 mm diameter of the truncated upper part) and a

glass petri dish (5 mm height and 25 mm diameter). The metal cone was glued to the bottom of the petri dish using the UV-curable glue. Prior to each measurement, the cone was filled with water up to its edge. For force measurements at the air–water interface, the petri dish was partially filled with water to reduce the evaporation from inside the cone. For force measurements at the oil–water interface, the petri dish was filled with n-hexadecane. In all cases, the fluid interface was practically flat and no curvature effects were considered. The liquid cell was then centered below the colloidal probe *via* an optical microscope and the cantilever speed was set to 1 μm s^{-1} to prevent any dynamic effects. At least 50 force–distance curves were collected for each automatic measurement.

Gel-trapping technique (GTT). The contact-angle distributions of monodisperse silica particles at the n-hexadecane–water interface were obtained following the procedure developed by Paunov.[19] The aqueous phase was 0.2–1 wt% solution of purified gellan gum, which is a non-adsorbing, gel-forming polysaccharide. To keep the gellan gum solution in a liquid state, the working solutions and glassware were pre-heated to *ca.* 50 °C in an oven. As a spreading solvent, an isopropanol–water mixture in 1:1 volume ratio was used. The silica particles were dispersed in the spreading solvent, so that their concentration was about 3 wt%.

Next, 2.5 mL of hot gellan gum solution were poured in a UV-ozone-cleaned glass petri dish (5 mm height and 25 mm diameter) and 2 mL of purified n-hexadecane were added over the aqueous gellan gum solution. Then, ∼2 μL of the silica suspension were taken with a micropipette and spread at the oil–water interface. Afterwards, the petri dish was slowly cooled for about 1 hour at 0.5 °C min^{-1} to achieve complete setting of the gel. Successively, a PDMS or a UV-glue replica of the particle–laden interface was created at 23 °C. The PDMS replica was cured for at least 48 hours, whereas the UV-glue replica was cured by 366 nm UV-light for 15 minutes. After curing, all replicas were carefully peeled off from the jellified aqueous phase, rinsed with water, dried and then sputtered with ∼10 nm-thick gold or platinum layers.

Using an optical 3D profilometer (PLu Neox; Sensofar, Spain) equipped with 50× confocal objective, we measured the height of the protruding particles, H_p, in each replica. The UV-glue was used in the case of hydrophilic silica particles, because of their inferior adhesion to the PDMS; see Fig. A1 and Appendix A1 for details in the ESI.† The error of the height measurement, due to the replica surface roughness, was always less than 150 nm. For each particle, using the measured H_p and the average particle radius R given by the supplier, $θ$ was calculated as follows:

$$θ = \arccos\left(\frac{H_p}{R} - 1\right) \tag{21}$$

Freeze-fracture shadow-casting (FreSCa) cryo-SEM method. We followed the procedure developed by Isa and co-workers[21,22] for contact-angle measurements at oil–water interfaces. 0.5 μL of water were first inserted into a custom-made copper holder with a 200 μm central depression. After that, 3 μL of purified n-decane containing the monodisperse silica particles were carefully deposited on top to create a particle–laden oil–water

interface at ambient temperature. The sample holder was then closed with a flat copper plate. To immobilize the particles in their equilibrium positions at the interface, the sample was shock-frozen in a liquid propane jet freezer (JFD 030; Bal-Tec AG/Leica, Germany) at a cooling rate of 30 000 K s^{-1}, leading to water vitrification. After vitrification, the samples were mounted under liquid nitrogen onto a double fracture cryo-stage and were transferred under a cryo-high-vacuum with a shuttle ($<5 \times 10^{-7}$ mbar; VCT010; Bal-Tec AG/Leica, Germany) to a pre-cooled freeze-fracture device at −120 °C (BAF060; Bal-Tec AG/Leica, Germany). The samples were then fractured and partially freeze-dried at −100 °C for 1 min to remove residual water condensation and ice crystals. Successively, at −120 °C, the particle–laden interfaces were coated by unidirectional tungsten deposition at an elevation angle of 30° to a thickness of 3 nm and by extra 2 nm with a continuously varying angle between 90° and 30°. The second deposition is necessary to minimize charging effects during imaging.

The freeze-fractured and metal-coated samples were transferred under high vacuum ($<5 \times 10^{-7}$ mbar) at −120 °C to a pre-cooled (−120 °C) cryo-SEM (Leo 1530 Gemini; Zeiss, Germany). Images were taken with a secondary-electron detector and $θ$ was extracted for individual particles as explained in ref. 22.

Drop shape analysis (DSA). We measured the static contact angles of water droplets on macroscopic planar solid surfaces that mimic the surfaces of non-modified/hydrophobized silica spheres, respectively. 1–3 μL water droplets were placed onto non-modified/hydrophobized silicon wafers immersed either in air, or in n-hexadecane. The three-phase contact angles of at least 5 droplets were measured using the Drop-Shape Analyzer (DSA100; Krüss GmbH, Germany).

4. Results and discussion

4.1. Numerical results

Here, we summarize the basic numerical results obtained from the theory in Section 2. Our main attention is devoted to the process of particle detachment from fluid interfaces (air–water and oil–water). Fig. 3 shows a sketch of a force–distance curve for the particle retraction process. For small particles in mechanical equilibrium, the fluid interface is flat and the net capillary force is zero. By pulling the particle upwards, the interface deforms, which results in a non-zero capillary force. Upon further pulling, the particle detaches from the interface and goes into the upper phase. From the retraction force–distance curve, we can determine: (i) the maximal force, F_{max}; (ii) the detachment distance, D_{max}; and (iii) the work for quasistatic detachment, W; see Fig. 3. These parameters are all related to the three-phase contact angle $θ$: F_{max} *via* eqn (2); D_{max} *via* eqn (3), (4) and (8); and W *via* eqn (6) – for explanations see Section 2.

The dependence of F_{max} on $θ$ was first derived by Scheludko & Nikolov[33] and is given by eqn (2). The distance D_{max} is defined as the maximal distance travelled by the particle center of mass from its equilibrium position to the point of detachment. Having determined D_{max}, we can calculate $θ$ from eqn (3), (4) and (8).
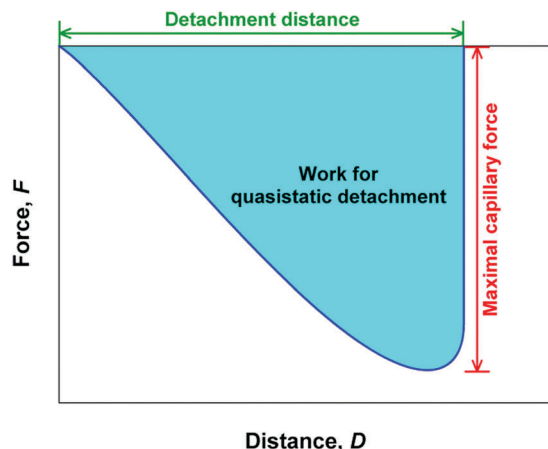
Fig. 3 Sketch of a force–distance curve for the process of particle retraction. From the $F(D)$ curve, we can directly extract: the maximal (capillary) force F_{max}, the detachment distance D_{max} and the work for quasistatic detachment W.

Fig. 4 Numerical results from the theory in Section 2. (a) The dimensionless detachment distance D_{max}/R vs. the three-phase contact angle θ. (b) The dimensionless work for quasistatic detachment $W/(\pi R^2 \sigma)$ vs. the three-phase contact angle θ. Each theoretical curve corresponds to a given Bond number ε in the range 2–14×10^{-4}, which encompasses our measurements.

Fig. 4a shows the dimensionless detachment distance D_{max}/R versus θ. As expected, D_{max}/R is larger for hydrophilic particles than for hydrophobic particles. For superhydrophobic particles $\theta \approx 180°$, D_{max}/R approaches zero. D_{max}/R decreases also when the Bond number $\varepsilon \equiv qR$ increases, that is, when either the particle radius, or the capillary length increase.

Another key parameter is the work for quasistatic detachment W, which is equal to the area over the $F(D)$ force–distance curve. The relationship between W and θ follows from eqn (6). In Fig. 4b, we see the numerical results for $W/(\pi R^2 \sigma)$ versus θ. Expectedly, $W/(\pi R^2 \sigma)$ is a decreasing function of θ and it approaches zero for superhydrophobic particles. Similarly to D_{max}/R, $W/(\pi R^2 \sigma)$ decreases when R increases. Physically, W coincides with the energy barrier associated with particle detachment (Fig. 2b). In Fig. 2b, the initial state coincides with the equilibrium position of the particle at the interface, while the transition state represents the fully stretched meniscus formed prior to particle detachment. Thus, W is analogous to the activation energy of chemical reactions.

An analytical expression for $W/(\pi R^2 \sigma)$ was found by Pitois & Chateau – eqn (7),[39] for the case of particle detachment under force control. However, in the regime of displacement control, the detachment happens when the distance D becomes equal to D_{max}. To take this difference into account (Fig. 5a), we derived the first-order correction $\Delta w^{(1)}$ expressed in eqn (15). Therefore, for quasistatic retraction under displacement control, $W/(\pi R^2 \sigma)$ should be evaluated either numerically from eqn (6), or analytically from eqn (19).

For the sake of comparison, in Fig. 5b, the analytical formulae for w_{PC} and $w^{(1)}$ from eqn (7) and (19) are compared to the exact numerical results as a function of the Bond number ε. We see that the closed-form expressions are quite accurate for very small Bond numbers ε, i.e. for very small particles. However, for larger particles, w_{PC} underestimates the quasistatic work for particle detachment by around 10%, whereas $w^{(1)}$ is more accurate and deviates less than 3% compared to the exact numerical calculations.
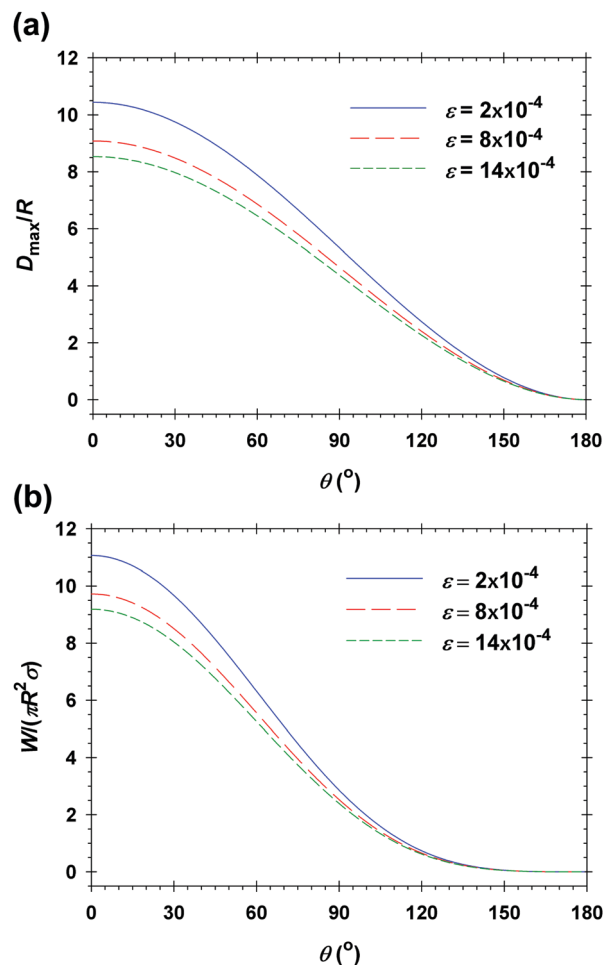
4.2. Colloidal-probe AFM results

Using colloidal-probe AFM, one can extract θ for individual smooth microparticles from various physical quantities. One of these quantities is the so-called jump-in distance δ,[43] which can be measured directly from the force–distance curves upon particle approach. For a sphere in its equilibrium position at the air–water or oil–water interface (having $\rho_{oil} < 1$ g cm^{-3}), δ represents the particle immersion depth into the aqueous phase and is related to θ as follows:[43]

$$\cos \theta = \frac{\delta}{R} - 1 \qquad (22)$$

Henceforth, the contact angle θ determined from the value of δ is denoted as θ_δ. Since δ is a parameter measured for the particle approach, θ_δ should give the advancing contact angle.

As explained in Section 4.1, the key parameters, which describe the particle retraction process, are: (i) the maximal force F_{max}; (ii) the detachment distance D_{max}; and (iii) the work for quasistatic detachment W. Hereafter, the receding contact
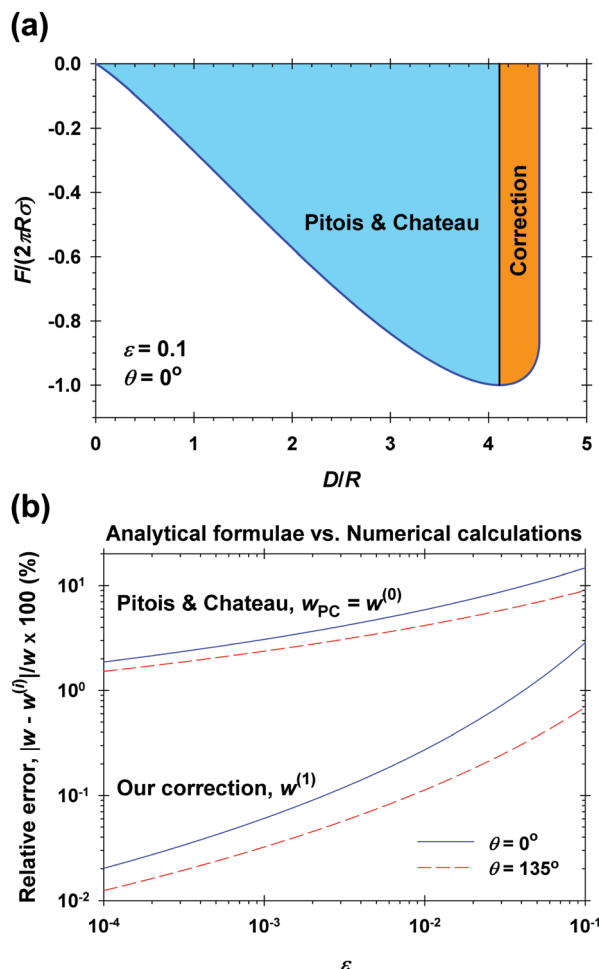
(a)

(b)

Fig. 5 (a) The plot represents a theoretical force–distance curve calculated for a large hydrophilic particle with $\theta = 0°$. The area over the curve (proportional to w) can be divided into two contributions: (i) up to the minimum – given by w_{PC} from eqn (7); and (ii) from the minimum to the detachment position – given by $\Delta w^{(1)}$ in eqn (15). (b) The relative errors of the analytical formulae [eqn (7) and (19)] for w are plotted as a function of the Bond number ε. The solid lines are for hydrophilic particles, $\theta = 0°$, and the dashed lines are for hydrophobic particles, $\theta = 135°$.

angles obtained from these physical quantities are designated as: θ_f, θ_d and θ_w, respectively.

Table 1 summarizes the three-phase contact angles of silica microspheres at both oil–water and air–water interfaces. θ and $\Delta\theta$ are calculated from at least 50 force–distance curves, unless a limited number of manual measurements are performed (first and last row in the table). Additional comments on the sources of errors are reported in Appendix A.2 in the ESI.† Expectedly, the advancing contact angle θ_δ is always higher than the receding contact angles θ_f, θ_d and θ_w. Compared to δ, which can be affected by hydrodynamic instabilities, capillary waves and fast wetting phenomena, F_{max}, D_{max}, and W seem to be more reproducible. Accordingly, the receding contact angles θ_f, θ_d and θ_w can all be determined quite accurately. Moreover, θ_f, θ_d and θ_w are also very close in value, which proves that the theoretical model from Section 2 is robust and self-consistent. Here, we should point out that θ_d is especially reliable since

Table 1 Three-phase contact angles θ of silica particles determined from the colloidal-probe AFM measurements using the theoretical model from Section 2. The subscripts of θ refer to the respective physical quantities. R is the particle radius. $\Delta\theta$ is the uncertainty of the contact angle, related to the standard deviations of F_{max}, D_{max} and W; see Appendix A.2 in the ESI for details

| R (μm)	θ_δ (°)	$\Delta\theta_\delta$ (°)	θ_f (°)	$\Delta\theta_f$ (°)	θ_d (°)	$\Delta\theta_d$ (°)	θ_w (°)	$\Delta\theta_w$ (°)
Oil–water (OW)								
5.62[a]	56	—	28	18[d]	42	—	33	—
1.50[b]	125	4	90	1	93	2	91	1
6.34[c]	142	2	120	1	121	1	117	2
3.75[c]	154	5	135	3	131	5	132	2
Air–water (AW)								
3.69[b]	71	—	58	10[d]	56	—	54	—

[a] Native (UV-cleaned) silica surface. [b] *In situ*-glue-modified silica surface. [c] Hydrophobized (fluorosilanized) silica surface. [d] Estimated value, assuming 10% relative error of F_{max}.

D_{max} depends only on the nanometric accuracy of the piezo-actuator and, in contrast to F_{max} and W, is independent of the cantilever calibration method.

Next, using Table 1, we will compare the wetting properties of the measured silica microspheres with different surface chemistry. The first silica particle, with $R = 5.62$ μm, is very hydrophilic since it was UV-ozone cleaned on the cantilever just before the AFM measurement. For such hydrophilic particles, part of the measurement was performed manually *via* a stepper-motor since D_{max} exceeded the maximal extension of the piezo-actuator. We thus have few force–distance curves, no correction for the deflection baseline and no consistent estimate for $\Delta\theta$. The second particle, with $R = 1.50$ μm, corresponds to a surface modified *in situ* by the UV-curable glue vapors during the colloidal probe preparation. This particle is more hydrophobic than native silica particles: $\theta_d = 93°$ *versus* $\theta_d = 42°$. The former value is very close to $\theta = 80 \pm 10°$ measured by DSA for water droplets on a glue-modified silicon wafer immersed in *n*-hexadecane. The third and fourth particles were hydrophobized following the procedure described in Section 3.2. Their average θ_d is $126 \pm 7°$, which agrees reasonably well with $\theta = 112 \pm 10°$ measured by DSA for water droplets on a hydrophobized silicon wafer immersed in *n*-hexadecane. The last particle, with $R = 3.69$ μm, measured at the air–water interface, is *in situ*-modified and hydrophilic with $\theta_d = 56°$. This contact angle is close to $\theta = 60 \pm 6°$ obtained by DSA measurements of water droplets on either non-modified, or glue-modified silicon wafers in air.

To demonstrate the validity of our theoretical model from Section 2, we calculated the force–distance curves for the particle retraction process without any adjustable parameters. Fig. 6 illustrates the comparison of four theoretical *versus* experimental force–distance curves, for which θ_d varies in a wide interval from 42° to 135°. Note that, θ_f and θ_d are determined for each $f(d)$ curve using only two points, and may slightly deviate from the average values in Table 1. The excellent agreement between theory and experiments (always within the experimental error) proves the adequacy of our model, which can be applied for contact-angle determination of individual microparticles.
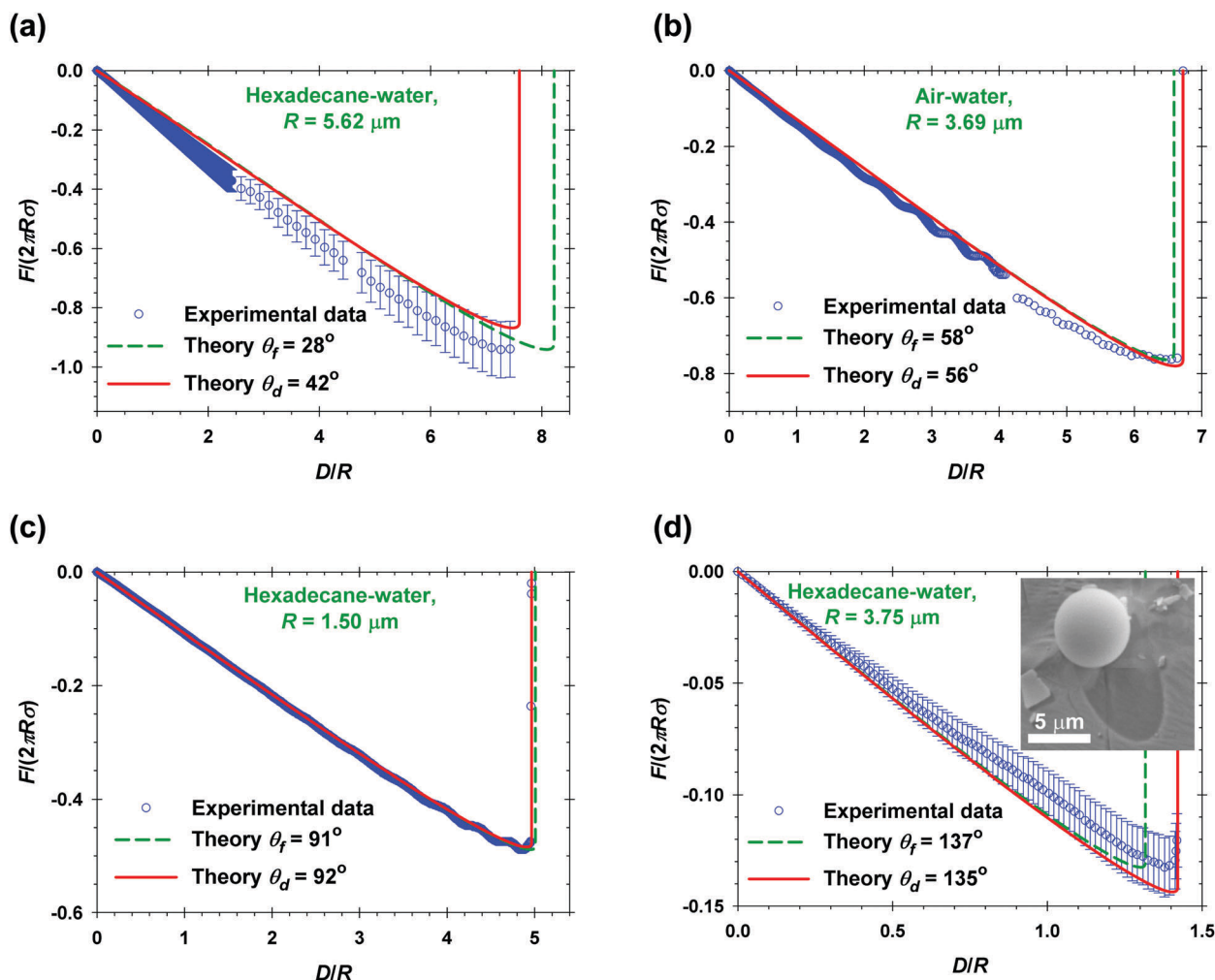
Fig. 6 Comparison of theoretical and experimental force–distance curves for the particle retraction process. The empty circles represent the experimental data, the dashed lines are calculated using θ_f and the solid lines are calculated using θ_d. All theoretical force–distance curves are evaluated without any adjustable parameters. The error bars in (a) and (d) correspond to 10% (relative) deviation in the AFM-measured force. The individual plots refer to: (a) A UV-ozone-cleaned silica particle at the n-hexadecane–water interface. (b) A hydrophilic silica particle at the air–water interface. (c) A glue-modified silica particle at the n-hexadecane–water interface. The *in situ*-modification takes place in the early stages of the glue curing. (d) A fluorosilanized silica particle at the n-hexadecane–water interface. The inset shows a FreSCa cryo-SEM image of such a particle with a contact angle of 137° at a n-decane–water interface.

To prove that the contact line motion on the particle surface before detachment fully determines the force–distance curves, we have produced a truncated silica sphere (Fig. 7a), cut by a focused ion beam (FIB), whose cut is positioned just below the expected detachment point. Fig. 7b shows that the theoretical and experimental force–distance curves practically coincide and $\theta_d = 101°$. As expected, the theory holds since the FIB-cut, with $\alpha_{cut} = 146°$, is just below the detachment point, $\alpha_{max,2} = 144°$. Thus, the contact line slides and then detaches before reaching the cut. If the FIB-cut were above the detachment point corresponding to a sliding contact line, then one would expect pinning at the edge.[44]

4.3. Comparison of different methods (AFM, GTT, FreSCa)

To verify the data obtained from colloidal-probe AFM, we applied two independent methods for contact-angle measurement: the gel-trapping technique (GTT) and the freeze-fracture shadow-casting (FreSCa) cryo-SEM method. Fig. 8 shows the three-phase contact angle distributions of non-modified and hydrophobized silica particles at the oil–water interface. The empty symbols represent the experimental points, whereas the solids lines are calculated assuming a normal distribution for θ: monomodal for the non-modified particles and bimodal for the hydrophobized particles. The presence of bimodal distributions can be ascribed to incomplete functionalization of a fraction of the particles. The cumulative distribution function (CDF) is:[45]

$$\mathrm{CDF} = \frac{\beta}{2}\left[1 + \mathrm{erf}\left(\frac{\theta - \theta_1}{\sqrt{2}\sigma_1}\right)\right] + \frac{1-\beta}{2}\left[1 + \mathrm{erf}\left(\frac{\theta - \theta_2}{\sqrt{2}\sigma_2}\right)\right], \quad (23)$$

where θ_1 and θ_2 are the mean contact angles of the two modes; σ_1 and σ_2 are their respective standard deviations; β and $1 - \beta$ are the weight fractions of each mode ($\beta = 1$ for monomodal distributions),
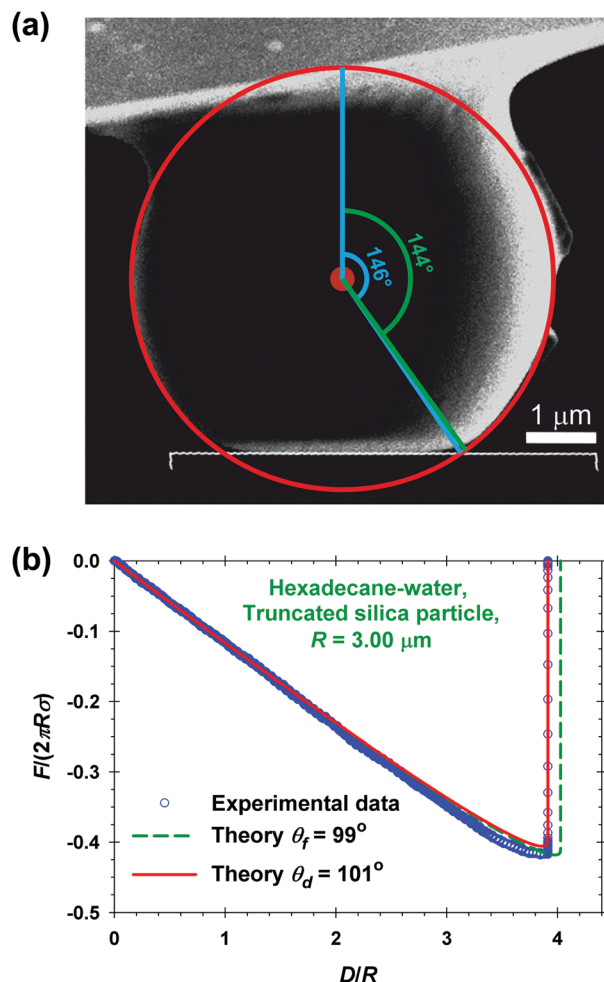
Fig. 7 (a) An SEM image of an FIB-truncated silica sphere attached to a tipless cantilever. The central angle, α_{cut}, which corresponds to the FIB-cut, is equal to 146°. (b) The plot shows the excellent agreement between the theoretical and experimental force–distance curves for a truncated (glue-modified) silica sphere at the n-hexadecane–water interface. The empty circles represent the experimental data, the dashed line is calculated using θ_f and the solid line is calculated using θ_d. The detachment process is theoretically described by a sliding contact line up to the detachment point, which is just above the FIB-cut. The two theoretical force–distance curves are calculated without any adjustable parameters.

and erf(x) is the error function. These five independent parameters were determined by non-linear fitting of the experimental data. Having determined the CDF in eqn (23), the probability density function (PDF) can be obtained by differentiation:[45]

$$\text{PDF} = \frac{d\text{CDF}}{d\theta}$$

$$= \frac{\beta}{\sqrt{2\pi}\sigma_1}\exp\left[-\left(\frac{\theta - \theta_1}{\sqrt{2}\sigma_1}\right)^2\right] + \frac{1 - \beta}{\sqrt{2\pi}\sigma_2}\exp\left[-\left(\frac{\theta - \theta_2}{\sqrt{2}\sigma_2}\right)^2\right].$$

(24)

The contact angles, θ_1 and θ_2, and their standard deviations, σ_1 and σ_2, are shown in Table 2.

From Table 2 and for a given surface modification (non-modified or hydrophobized particles), we see that the average

contact angles obtained from GTT and FreSCa are in good agreement as they differ within the respective standard deviations. The next step is to compare the colloidal-probe AFM to GTT and FreSCa. Before that, however, it should be noted that using the colloidal-probe AFM we measure θ for individual particles, whereas using GTT and FreSCa we obtain contact angle distributions, thus also capturing particle-to-particle variations. Having that in mind, the contact angle θ_d for non-modified silica spheres is close to the average contact angle determined from GTT and is slightly higher than the one from FreSCa. For hydrophobized silica spheres, θ_d practically coincides with θ_2, which corresponds to the completely fluorosilanized particle surface. During fluorosilane-vapor deposition, however, some of the particles are only partially hydrophobized and their average contact angle is given by θ_1.

In summary, by applying independent experimental techniques, we prove that our theoretical model is robust and self-consistent, and can be used to determine θ in a reliable way.

5. Summary and conclusions

In this paper, we have developed a detailed theoretical model to interpret the experimental data from colloidal-probe AFM that describes the process of particle detachment from the interface. For small spherical particles in mechanical equilibrium, the fluid interface is flat and the net capillary force is zero. By pulling the particle upwards, the interface deforms, which results in a non-zero capillary force. At some point, the particle detaches from the interface and goes into the upper phase. From the force–distance curve, we can directly extract: (i) the maximal force F_{max}; (ii) the detachment distance D_{max}; and (iii) the work for quasistatic detachment W. These parameters are all related to the three-phase contact angle θ.

F_{max} is a decreasing function of θ and was first calculated by Scheludko & Nikolov.[33] Similarly, D_{max}/R and $W/(\pi R^2\sigma)$ decrease with θ and both approach zero for super-hydrophobic particles $\theta \approx 180°$. In contrast to F_{max}, which is independent of the Bond number $\varepsilon \equiv qR$, D_{max}/R and $W/(\pi R^2\sigma)$ both decrease when ε increases, namely, when the particle radius R increases. Physically, W can be interpreted as an energy barrier for particle detachment in analogy to the activation energy for chemical reactions. We devised a very accurate closed-form expression for W, which improves those found by Pitois & Chateau.[39,40]

Using F_{max}, D_{max} and W, as well as our theoretical model, we calculated the receding contact angles θ_f, θ_d and θ_w for non-modified and hydrophobized silica particles at both air–water and oil–water interfaces. The advancing contact angle θ_δ was evaluated from the so-called jump-in distance δ,[43] which was measured upon particle approach. As expected, the advancing contact angle θ_δ is higher than the receding contact angles θ_f, θ_d and θ_w. It is important to stress here that θ_f, θ_d and θ_w can all be determined very accurately and are very close in value, which proves that our theoretical model is adequate and self-consistent.

Furthermore, our model was validated in three ways. First, we calculated the theoretical force–distance curves without using any adjustable parameters and they closely coincide with
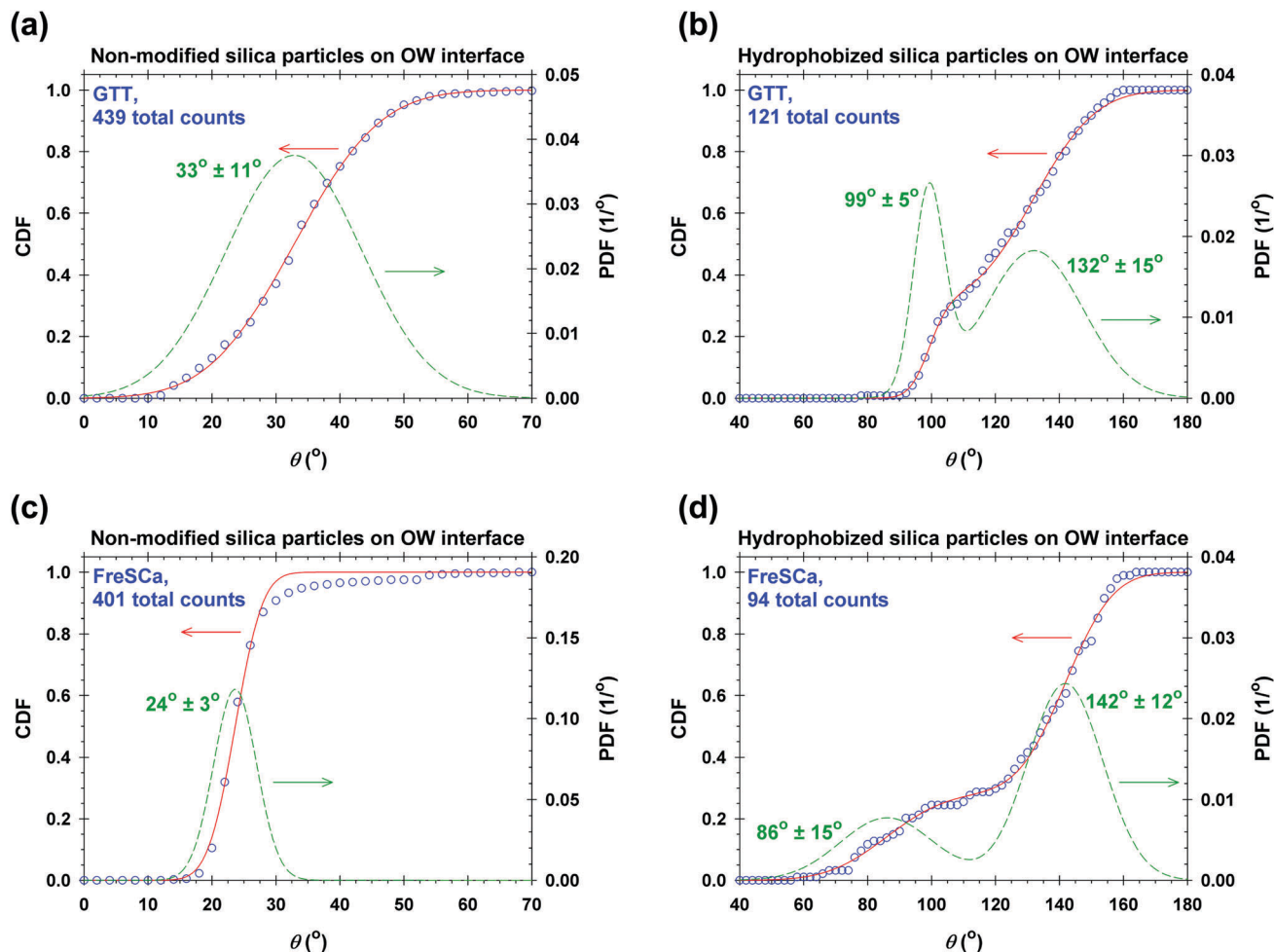
Fig. 8 Three-phase contact angle distributions of non-modified/hydrophobized silica particles at the oil–water (OW) interface. The distributions in terms of CDF (solid line) and PDF (dashed line) are calculated after statistical analysis of our experimental data (empty circles) from the gel-trapping technique (GTT) and the freeze-fracture shadow-casting (FreSCa) cryo-SEM method. Using GTT, we obtained the contact-angle distributions for (a) non-modified and (b) hydrophobized silica particles. Using FreSCa, we obtained the contact-angle distributions for the same batch of (c) non-modified and (d) hydrophobized silica particles.

Table 2 Comparison of the contact angles θ of smooth silica microparticles at the oil–water interface determined from independent methods: colloidal-probe AFM, the gel-trapping technique (GTT) and the freeze-fracture shadow-casting (FreSCa) cryo-SEM method. The silica spheres have different surface chemistry: non-modified vs. hydrophobized particles. From the colloidal-probe AFM, we presented the values for θ_d. For GTT and FreSCa, the contact angle distributions are shown in Fig. 8. Here, the mean values and standard deviations are listed

Silica particles	Contact angle, θ (°)		
	AFM	GTT	FreSCa
Non-modified	42	33 ± 11	24 ± 3
Hydrophobized	126 ± 7	99 ± 5 (θ_1)	86 ± 15 (θ_1)
		132 ± 15 (θ_2)	142 ± 12 (θ_2)

the experimental data for a wide range of contact angles. Second, as a proof of concept, the model was successfully applied to predict the experimental force–distance curve of an FIB-truncated sphere, whose FIB-cut is positioned below the point of particle detachment from the interface. Third, using independent experimental methods such as GTT, FreSCa and DSA, we verified the contact angle measurements by AFM.

The results contribute to the understanding of particle wetting, adhesion and detachment from fluid interfaces. Additionally, the theoretical model can be applied to predict both the force and interfacial deformation imparted by the colloidal probe, which is especially valuable when AFM is used as a tool for guided particle assembly. As an outlook, we foresee the extension of this model to the case of fixed contact line (pinned contact line),[44] as this is commonly found in many particle systems used in applications, e.g. showing surface roughness for enhanced emulsion stability.[46]

Acknowledgements

References

1 S. U. Pickering, *J. Chem. Soc., Trans.*, 1907, **91**, 2001–2021.

2 R. Aveyard, B. P. Binks and J. H. Clint, *Adv. Colloid Interface Sci.*, 2003, **100–102**, 503–546.

3 A. D. Dinsmore, M. F. Hsu, M. G. Nikolaides, M. Marquez, A. R. Bausch and D. A. Weitz, *Science*, 2002, **298**, 1006–1009.

4 A. Verma and F. Stellacci, *Small*, 2010, **6**, 12–21.

5 A. V. Nguyen, R. J. Pugh and G. J. Jameson, in *Colloidal Particles at Liquid Interfaces*, ed. B. P. Binks and T. S. Horozov, Cambridge University Press, Cambridge, 1st edn, 2006, ch. 9, pp. 328–382.

6 K. P. Velikov and O. D. Velev, in *Colloidal Particles at Liquid Interfaces*, ed. B. P. Binks and T. S. Horozov, Cambridge University Press, Cambridge, 1st edn, 2006, ch. 7, pp. 225–297.

7 D. J. Norris, E. G. Arlinghaus, L. Meng, R. Heiny and L. E. Scriven, *Adv. Mater.*, 2004, **16**, 1393–1399.

8 A. Böker, J. He, T. Emrick and T. P. Russell, *Soft Matter*, 2007, **3**, 1231–1248.

9 R. McGorty, J. Fung, D. Kaz and V. N. Manoharan, *Mater. Today*, 2010, **13**, 34–42.

10 L. Isa, K. Kumar, M. Müller, J. Grolig, M. Textor and E. Reimhult, *ACS Nano*, 2010, **4**, 5665–5670.

11 B. M. Rey, R. Elnathan, R. Ditcovski, K. Geisel, M. Zanini, M. A. Fernandez-Rodriguez, V. V. Naik, A. Frutiger, W. Richtering, T. Ellenbogen, N. H. Voelcker and L. Isa, *Nano Lett.*, 2016, **16**, 157–163.

12 A. F. Koretsky and P. M. Kruglyakov, *Izv. Sib. Otd. Akad. Nauk SSSR, Ser. Biol. Nauk*, 1971, **2**, 139.

13 B. P. Binks and T. S. Horozov, in *Colloidal Particles at Liquid Interfaces*, ed. B. P. Binks and T. S. Horozov, Cambridge University Press, Cambridge, 1st edn, 2006, ch. 1, pp. 1–74.

14 T. S. Horozov, R. Aveyard, J. H. Clint and B. P. Binks, *Langmuir*, 2003, **19**, 2822–2829.

15 Y. Peng, W. Chen, T. M. Fischer, D. A. Weitz and P. Tong, *J. Fluid Mech.*, 2009, **618**, 243–261.

16 J. T. Petkov, K. D. Danov, N. D. Denkov, R. Aust and F. Durst, *Langmuir*, 1996, **12**, 2650–2653.

17 P. A. Kralchevsky and K. Nagayama, *Langmuir*, 1994, **10**, 23–36.

18 M. Zanini and L. Isa, *J. Phys.: Condens. Matter*, 2016, **28**, 313002.

19 V. N. Paunov, *Langmuir*, 2003, **19**, 7970–7976.

20 L. N. Arnaudov, O. J. Cayre, A. C. Stuart, D. Stoyanov, M. A. C. Stuart, S. D. Stoyanov and V. N. Paunov, *Phys. Chem. Chem. Phys.*, 2010, **12**, 328–331.

21 L. Isa, F. Lucas, R. Wepf and E. Reimhult, *Nat. Commun.*, 2011, **2**, 438–457.

22 L. Isa, *Chimia*, 2013, **67**, 231–235.

23 N. Vogel, J. Ally, K. Bley, M. Kappl, K. Landfester and C. K. Weiss, *Nanoscale*, 2014, **6**, 6879–6885.

24 A. Hadjiiski, R. Dimova, N. D. Denkov, I. B. Ivanov and R. Borwankar, *Langmuir*, 1996, **12**, 6665–6675.

25 T. S. Horozov, D. A. Braz, P. D. I. Fletcher, B. P. Binks and J. H. Clint, *Langmuir*, 2008, **24**, 1678–1681.

26 D. O. Grigoriev, J. Krägel, V. Dutschk, R. Miller and H. Möhwald, *Phys. Chem. Chem. Phys.*, 2007, **9**, 6447–6454.

27 B. P. Binks, J. H. Clint, A. K. F. Dyab, P. D. I. Fletcher, M. Kirkland and C. P. Whitby, *Langmuir*, 2003, **19**, 8888–8893.

28 T. N. Hunter, G. J. Jameson and E. J. Wanless, *Aust. J. Chem.*, 2007, **60**, 651–655.

29 M. Preuss and H.-J. Butt, *J. Colloid Interface Sci.*, 1998, **208**, 468–477.

30 G. Gillies, K. Büscher, M. Preuss, M. Kappl, H.-J. Butt and K. Graf, *J. Phys.: Condens. Matter*, 2005, **17**, S445–S464.

31 D. M. Kaz, R. McGorty, M. Mani, M. P. Brenner and V. N. Manoharan, *Nat. Mater.*, 2011, **11**, 138–142.

32 H.-J. Butt, B. Cappella and M. Kappl, *Surf. Sci. Rep.*, 2005, **59**, 1–152.

33 A. D. Scheludko and A. D. Nikolov, *Colloid Polym. Sci.*, 1975, **253**, 396–403.

34 A. Scheludko, B. V. Toshev and D. T. Bojadjiev, *J. Chem. Soc., Faraday Trans. 1*, 1976, **72**, 2815–2828.

35 B. V. Derjaguin, *Dokl. Akad. Nauk SSSR*, 1946, **51**, 517.

36 D. F. James, *J. Fluid Mech.*, 1974, **63**, 657–664.

37 L. L. Lo, *J. Fluid Mech.*, 1983, **132**, 65–78.

38 P. A. Kralchevsky, I. B. Ivanov and A. D. Nikolov, *J. Colloid Interface Sci.*, 1986, **112**, 108–121.

39 O. Pitois and X. Chateau, *Langmuir*, 2002, **18**, 9751–9756.

40 X. Chateau and O. Pitois, *J. Colloid Interface Sci.*, 2003, **259**, 346–353.

41 G. E. Yakubov, O. I. Vinogradova and H.-J. Butt, *J. Adhes. Sci. Technol.*, 2000, **14**, 1783–1799.

42 J. L. Hutter and J. Bechhoefer, *Rev. Sci. Instrum.*, 1993, **64**, 1868–1873.

43 M. Preuss and H.-J. Butt, *Int. J. Miner. Process.*, 1999, **56**, 99–115.

44 J. Ally, M. Kappl and H.-J. Butt, *Langmuir*, 2012, **28**, 11042–11047.

45 B. S. Everitt and D. J. Hand, *Finite Mixture Distributions*, Chapman & Hall, London, 1981.

46 R. Van Hooghten, L. Imperiali, V. Boeckx, R. Sharma and J. Vermant, *Soft Matter*, 2013, **9**, 10791–10798.